J. Electrochem. Sci. Eng. **16** (2026) 3163; https://doi.org/10.5599/jese.3163

Open Access : : ISSN 1847-9286
https://pub.iapchem.org/ojs/index.php/JESE

Original scientific paper

Nickel hydroxide enhanced nickel selenides for oxygen evolution reaction

Francisco J. García-Partida[1,2], Ricardo Briones-Martínez[1,2], Eduardo M. Sánchez[1], Salomé M. de la Parra Arciniega[1], Rodrigo Mayen-Mondragon[3] and Nora A. Garcia-Gomez[1,2,✉]

[1]*Facultad de Ciencias Químicas, FCQ, Universidad Autónoma de Nuevo León, Av. Universidad s/n Cd. Universitaria, San Nicolás de los Garza, Nuevo León, 66455, México*
[2]*Centro de Investigación en Biotecnología y Nanotecnología, CIBYN, Universidad Autónoma de Nuevo León, Parque de Investigación e Innovación Tecnológica, PIIT, Apodaca, Nuevo León, 66600, México*
[3]*UNITA, Universidad Nacional Autónoma de México, Vía de la Innovación 410, PIIT-Monterrey Autopista Monterrey km 10, Apodaca 66628, Nuevo León, México*

*Corresponding Author: E-mail: ✉nora.garcian@uanl.edu.mx

Received: November 11, 2025; Accepted February 26, 2026; Published: February xx, 2026

Abstract

Transition to sustainable energy systems relies on the development of efficient and cost-effective hydrogen production technologies. A major challenge in this field is designing high-performance electrocatalysts based on earth-abundant, low-cost materials. In this work, three nickel selenide phases, $NiSe_2$, NiSe, and Ni_3Se_2, along with their corresponding $Ni(OH)_2$-modified heterostructures, were synthesized on nickel foam and systematically evaluated as oxygen evolution reaction (OER) electrocatalysts in alkaline media. X-ray diffraction and scanning electron microscopy analyses revealed that the incorporation of $Ni(OH)_2$ profoundly influenced nucleation pathways and promoted more homogeneous active-phase distribution across the three-dimensional substrate. Electrochemical characterization demonstrated that all $Ni(OH)_2$-modified electrodes exhibited enhanced catalytic performance compared to their unmodified counterparts. Among them, NiSe-OH supported on nickel foam, referred to as NiSe-OH/NF, achieved the lowest overpotential of 177 mV at 10 mA cm^{-2} and displayed favourable reaction kinetics, as reflected by its Tafel slope. The improved activity was attributed to synergistic interactions between Ni and Se, the activation of the $Ni(OH)_2$/NiOOH redox couple, and optimized charge-transfer pathways facilitated by the heterostructured interface. Long-term stability tests confirmed that the hybrid catalysts maintained over 86 % of their maximum current density after extended operation. These results establish Ni-Se/$Ni(OH)_2$ heterostructures as promising, earth-abundant materials for efficient alkaline OER and offer new insights into interface engineering for next-generation electrocatalyst design.

Keywords

Alkaline water splitting; electrocatalysts; heterostructured interfaces; transition metal chalcogenides.

Introduction

Hydrogen is a versatile gas with a wide range of industrial and technological applications, such as the chemical and refining industries, metalworking, electronics manufacturing, food processing, medicine, and energy storage. In particular, hydrogen energy storage provides an alternative to conventional chemical energy systems, as electrical power can be converted into hydrogen, a process uniquely suited for storing and transporting renewable energy. This capability positions hydrogen as a key component in the global energy transition [1]. The stored energy can subsequently be released by using hydrogen as fuel in engines, turbines, or fuel cells [2,3], the latter being notably more efficient than traditional combustion engines.

Among the available hydrogen production methods, electrolysis is considered the most effective due to the abundance of water available and the absence of polluting by-products. Water splitting involves two half-reactions: the hydrogen evolution reaction (HER) at the cathode and the oxygen evolution reaction (OER) at the anode. The OER is generally regarded as the rate-limiting step, involving four proton-coupled electron transfer reactions ($4OH^- \rightarrow O_2 + 2H_2O + 4e^-$) under alkaline conditions, and requiring a large anodic potential [4-7]. Historically, precious metal oxides, such as IrO_2 and RuO_2, have been the most effective OER catalysts due to their high stability and low overpotential, with values around 300 mV at a current density of 10 mA cm^{-2} [8]. However, the scarcity and high cost of noble metals such as iridium and ruthenium hinder large-scale commercialization of green hydrogen production. Consequently, the development of inexpensive and highly active electrocatalysts remains a major challenge.

Extensive research over the past decades has focused on designing cost-effective, earth-abundant, and efficient electrocatalysts. Special attention has been devoted to transition metal compounds, particularly those in the same periodic groups as platinum. Recent studies have identified a range of non-precious metal compounds as promising alternatives, including transition metal, chalcogenides [9,10] such as sulphides [11], selenides [12], and phosphides [13]. Among them, selenides have attracted growing interest owing to their relatively low intrinsic electrical resistivity, which facilitates charge-transfer kinetics, as well as selenides based on cobalt [14], nickel [15], and iron [16].

To further enhance their catalytic performance, researchers are exploring methods to support these materials on different conductive substrates, such as carbon nanotubes [17], nickel foam [18,19], carbon cloth [20] and gold sheets [21], which improve electrical conductivity and increase the number of exposed active sites. Additionally, various synthesis and deposition techniques, including hydrothermal growth [22], electrochemical deposition [23] and selenization [24,25], have been explored to tailor the morphology and crystal structure of the catalysts.

Nickel selenides have been extensively reported as efficient OER catalysts, with the main crystalline phases of nickel selenide: $NiSe_2$ (cubic), NiSe (hexagonal), and Ni_3Se_2 (trigonal). For instance, Huang *et al*. synthesized a reduced graphene oxide and nickel selenide (Ni_3Se_2) nanoforest decorated on nickel foam *via* a hydrothermal method, achieving an overpotential of 292.61 mV at 10 mA cm^{-2} in a basic medium of 1.0 M KOH [22]. Arabi *et al*. [23] reported the obtention of nanoporous NiSe films by electrodeposition on graphite rods, which exhibited an overpotential of 268 mV at 10 mA cm^{-2}. This performance has been widely attributed to the well-defined nanoporous morphology, which provides a large number of active sites, and to the synergistic effect between Ni and Se atoms, which enhances intrinsic catalytic activity. Esmailzadeh *et al*. [15] reported the synthesis of $NiSe_2$ and NiSe supported on a Ni foam by electrodeposition. These materials exhibit strong OER activity, as evidenced by low overpotentials of 235 and 287 mV at 10 mA cm^{-2} in

1.0 M KOH, respectively, and excellent stability over 500 cycles. These findings consistently highlight the superior catalytic properties of nickel selenide compounds for OER.

The electrocatalytic activity of nickel-based materials in alkaline medium is often attributed to the formation of the $Ni(OH)_2$/NiOOH redox couple. In this context, nickel selenide, which can easily form NiOOH at lower potentials, tends to exhibit enhanced OER performance [26,27]. Ghosh *et al*. [26] demonstrated that $NiSe_2$ nanoflakes grown on carbon cloth act as an efficient ORR pre-catalyst, requiring an overpotential of only 210 mV to reach 10 mA cm^{-2} in an alkaline medium. Furthermore, they attributed this high activity to the *in situ* formation of a nickel hydroxide active layer on the material's surface, supported by the conductive $NiSe_2$ core. Conversely, Swesi *et al*. [28] reported that textured NiSe films exhibited a superior activity for OER compared to intentionally prepared $Ni(OH)_2$ films, achieving an overpotential of only 140 mV at 10 mA cm^{-2} in alkaline medium, post-catalysis characterization confirmed the structural integrity of the $NiSe_2$ phase, indicating that its catalytic activity is an intrinsic property of the selenide and does not depend on the formation of a hydroxide redox couple.

While the synergistic interplay between the conductive selenide phases and active hydroxide layers is well established, the long-term evolution and stability of such composite interfaces under continuous operation remain insufficiently understood. Moreover, the combined effect of different nickel selenide phases coexisting on the same support has not yet been systematically investigated.

The present work compares different nickel selenide phases supported on nickel foam (NF) to evaluate the effect of $Ni(OH)_2$ on their catalytic activity for the oxygen evolution reaction. The results revealed that the samples containing $Ni(OH)_2$ exhibited lower overpotentials than their hydroxide-free analogues.

Experimental

Chemicals

Acetone absolute (CTR Scientific, Monterrey, N.L., Mexico), sulfuric acid 93 to 98 % (CTR Scientific, Monterrey, N.L., Mexico), ethylenediaminetetraacetic acid ≥99 % (Sigma-Aldrich, San Luis, MO, USA), selenium powder ≥99.50 % (Sigma-Aldrich, San Luis, MO, USA), nickel (II) chloride hexahydrate (Sigma-Aldrich, San Luis, MO, USA), hydrochloric acid (ACS Reagent, Sigma-Aldrich, San Luis, MO, USA), nickel foam 99.8 % (Shenzhen, Hong Kong) were used as received without further treatment or purification. Selenium dioxide (SeO_2) was synthesized by oxidizing powdered selenium with H_2SO_4, followed by evaporation and recrystallization through triple sublimation. The Ni foam substrates were cleaned by immersion in 0.5 M HCl for 15 min, rinsed thoroughly with deionized water, and subsequently washed with acetone to remove any organic residues.

Sample preparation

Synthesis of $Ni(OH)_2$/nickel foam

$Ni(OH)_2$/NF nanocomposites were prepared by the hydrothermal method. In a typical experiment, a 1 cm^2 piece of Ni foam was immersed in a 31 mL aqueous solution of a 0.10 mM $NiCl_2$ inside a Teflon-lined stainless-steel autoclave and heated at 180 °C for 18 h under a vapor pressure of 1 kg cm^{-2}. The resulting foam was repeatedly washed with water and dried at 60 °C (20GC, Quincy Lab, Columbia, USA). The $Ni(OH)_2$/NF obtained was used as a substrate for the synthesis of nickel selenide "-OH", in which the selenium source and reaction conditions were varied.

Synthesis of Ni_3Se_2-OH/nickel foam and Ni_3Se_2/nickel foam

Ni_3Se_2-OH/NF was obtained by annealing $Ni(OH)_2$/NF at 550 °C for 1 h under a nitrogen atmosphere, with Se powder placed upstream in the gas flow to promote sublimation and subsequent reaction over the substrate. Ni_3Se_2/NF was synthesized under identical conditions using pristine Ni foam instead of $Ni(OH)_2$/NF.

Synthesis of NiSe-OH/nickel foam and NiSe/nickel foam

20 mg of selenium powder was dissolved in 1 mL of deionized water, followed by the addition of 100 mg of $NaBH_4$. The mixture was stirred until a crystalline solution was obtained, then transferred to a Teflon-lined autoclave containing 30 mL of ethanol and a $Ni(OH)_2$/NF substrate. The reaction was conducted at 140 °C for 12 h under a vapor pressure of 1 kg cm^{-2}. Afterward, the samples were thoroughly washed with water and dried at 60 °C. NiSe/NF was synthesized under the same conditions, except that pristine Ni foam was used directly instead $Ni(OH)_2$/NF.

Synthesis of $NiSe_2$-OH/nickel foam and $NiSe_2$/nickel foam

$NiSe_2$/NF was obtained by placing a $Ni(OH)_2$/NF piece in a Teflon-lined autoclave containing 31 mL of an aqueous solution of 0.25 mM of selenium powder, 0.65 M of KOH, and 1.60 mM of EDTA. The autoclave was maintained at 160 °C for 10 h under a vapor pressure of 1 kg cm^{-1}. The resulting sample was washed repeatedly with water and dried at 60 °C. $NiSe_2$/NF was prepared under identical conditions using pristine Ni foam as the substrate.

Characterization

The morphology and microstructure of the materials were examined using a JEOL scanning electron microscope operated at 15 keV. Phase identification and crystal structure analysis were performed by X-ray diffraction (XRD) using a Bruker D2 Phaser diffractometer equipped with Cu-Kα (λ = 0.15418 nm. Diffraction patterns were recorded over a 2θ angle from 12 to 90°, with a step of 0.05 and a dwell time of 0.5 s per step. Phase assignments were made by comparison with the PDF-2 database (ICDD International Centre for Diffraction Data)[29].

Electrochemical measurements

The electrocatalytic performance of the synthesized materials toward the OER was evaluated in a standard three-electrode configuration using a potentiostat/galvanostat (VMP3 Biologic Science Instruments). The nickel foam-based materials were used directly as working electrodes, with a defined geometric area of 1 cm^2 [30], with Hg/HgO (NaOH 1.0 M) and a platinum twisted wire were used as reference and counter electrodes, respectively.

All measured potentials were converted to the reversible hydrogen electrode (RHE) scale using the Nernst equation (Equation (1)):

$$E_{RHE} = E_{Hg/HgO} + (0.059pH) + 0.965 \quad (1)$$

where E_{RHE} is the potential *versus* RHE and $E_{Hg/HgO}$ is the potential measured *versus* Hg/HgO reference electrode.

Prior to OER testing, electrodes were activated by performing a cyclic voltammetry (CV) at a scan rate of 50 mV s^{-1} until a stable response was achieved. Linear sweep voltammetry (LSV) was performed in 1.0 M KOH at a scan rate of 5 mV s^{-1}. The catalytic performance was normalized by the geometric surface area. The estimation of electrochemically active surface area (ECSA) *via* double-layer capacitance (C_{dl}) was excluded, as standard 2D models often yield overestimated values for high-porosity 3D foam electrodes [9].

The overpotential (η) was determined using Equation (2), defined as the difference between the potential measured against RHE and the standard theoretical voltage for water electrolysis (1.229 V):

$$\eta = E_{RHE} - 1.229\ V \quad (2)$$

Catalyst stability toward OER was evaluated using chronoamperometry (CA) and cyclic voltammetry (CV).

Results and discussion

Figure 1 presents the X-ray diffraction patterns of $NiSe_2$-OH/NF, $NiSe_2$/NF, NiSe-OH/NF, NiSe/NF, Ni_3Se_2-OH/NF, and Ni_3Se_2/NF. All diffractograms display three prominent reflections at 2 θ values of 44.5, 51.9 and 76.5°, corresponding to the {111}, {200}, and {220} crystallographic planes of metallic Ni foam substrate (PDF NIST-065-2865). The high intensity of these reflections confirms strong X-ray penetration through the porous structure of the samples containing $Ni(OH)_2$ exhibit additional diffraction peaks at 2θ angle 19.3, 33.1, 38.6, 59.1 and 62.8°, which are indexed to the β-phase of $Ni(OH)_2$ (PDF ICDD-014-0117), corresponding to the {001}, {100}, {101}, {110}, and {111} planes, respectively. The β-$Ni(OH)_2$ phase originates from the oxidation of Ni foam in a 0.10 mM $NiCl_2$ solution. The formation mechanism involves the generation of a Ni aquo complex, followed by the formation of hydroxide ions from dissolved oxygen, ultimately leading to $Ni(OH)_2$ precipitation [31], as described by Equations (3) to (5).

$$NiCl_2 + nH_2O \rightarrow [Ni(H_2O)_n]^{2+} + 2Cl^- \quad (3)$$

$$O_2 + 2H_2O + 4e^- \rightarrow 4OH^- \quad (4)$$

$$[Ni(H_2O)_n]^{2+} + 2OH^- \rightarrow Ni(OH)_2 + nH_2O \quad (5)$$

Distinct XRD patterns confirmed the successful formation of different nickel selenide phases depending on the synthesis route. For $NiSe_2$/NF (Figure 1A), the diffractogram reflections correspond to both metallic Ni and the cubic phase of $NiSe_2$ (PDF ICDD-041-1495), with characteristic reflections at 2θ = 29.8, 33.4, 36.7, 50.5, 55.3 and 57.6° indexed to the (200), (210), (211), (311), (230) and (321) planes, respectively.

For the $NiSe_2$-OH/NF sample (Figure 1B), three sets of reflections are observed. The first corresponds to metallic Ni, the second to cubic $NiSe_2$ (PDF ICDD-041-1495) with reflections at 2θ of 29.8, 33.4, 36.7, 50.5, 55.3 and 57.6°, while a weaker peak at 19.3° corresponds to the (001) plane of β-$Ni(OH)_2$ (PDF ICDD-014-0177). The formation of $NiSe_2$-OH/NF involves the oxidation of Ni foam to generate Ni^{2+} ions, which subsequently coordinate with EDTA to form the NiY^{2-} complex. Simultaneously, SeO_2 undergoes hydrolysis and reduction to form Se^{2-} species that react with Ni^{2+} to yield $NiSe_2$ [32]. The formation mechanism can be summarized by Equations (6) to (9):

$$SeO_2 + H_2O \rightarrow H_2SeO_3 \quad (6)$$

$$H_2SeO_3 + 4H^+ + 4e^- \rightarrow Se + 3H_2O \quad (7)$$

$$Se + 2H+ + 2e- \rightarrow H_2Se \quad (8)$$

$$H_2Se + Se + Ni_2^+ \rightarrow NiSe_2 + 2H^+ \quad (9)$$

For NiSe/NF (Figure 1C), the diffraction reflections indicate three main phases: metallic Ni, the hexagonal NiSe phase (PDF ICDD-002-0892) with reflections at 2θ of 32.8, 49.9 and 59.6° corresponding to (101), (110), and (103) planes, and non-stoichiometric hexagonal phase $Ni_{0.95}Se$ (PDF ICSD-072-2546) with a weak reflection at 32.9°. The latter likely results from localized Ni deficiency during crystal growth, as supported by SEM observations (Figure 2c), which show separated crystal growth, suggesting limited Ni diffusion.

The NiSe-OH/NF sample (Figure 1D) exhibits characteristic reflections from metallic Ni, hexagonal NiSe, and β-$Ni(OH)_2$ (PDF ICDD-014-0177) with peaks at 2θ of 19.3, 38.6, 52.1 and 59.1° corresponding to (001), (101), (102), and (110) planes, respectively. The proposed formation mechanism of

NiSe-OH/NF begins with the reduction of Se by $NaBH_4$ in aqueous solution, producing Se^{2-} and borate species. On the other hand, the H^+ from boric acid oxidizes the Ni foam to Ni^{2+} ions, which then react with the Se^{2-} ions to form NiSe. The reactions are given by Equations (10) to (12) [33]:

$$BH^{4-} + Se + H_2O \rightarrow H^+ + Se^{2-} + BO_3^{3-} \quad (10)$$

$$H^+ + Ni \rightarrow Ni^{2+} + H_{2(g)} \quad (11)$$

$$Ni^{2+} + Se^{2-} \rightarrow NiSe_{(s)} \quad (12)$$

For the sample of Ni_3Se_2/NF (Figure 1E), only metallic Ni reflections are detected with no evidence of crystalline selenide or oxide phases. However, the presence of rod like, sphere-aggregated structures in SEM (Figure 2D) suggests that the nickel selenide is amorphous or that its reflections are masked by the intense signals of Ni with high crystallinity. In contrast, the Ni_3Se_2-OH/NF sample (Figure 1F) exhibits distinct phases: metallic Ni (PDF NIST-065-2865), β-$Ni(OH)_2$ (PDF ICDD-014-0117) and trigonal Ni_3Se_2 (PDF ISCD-077-3110).

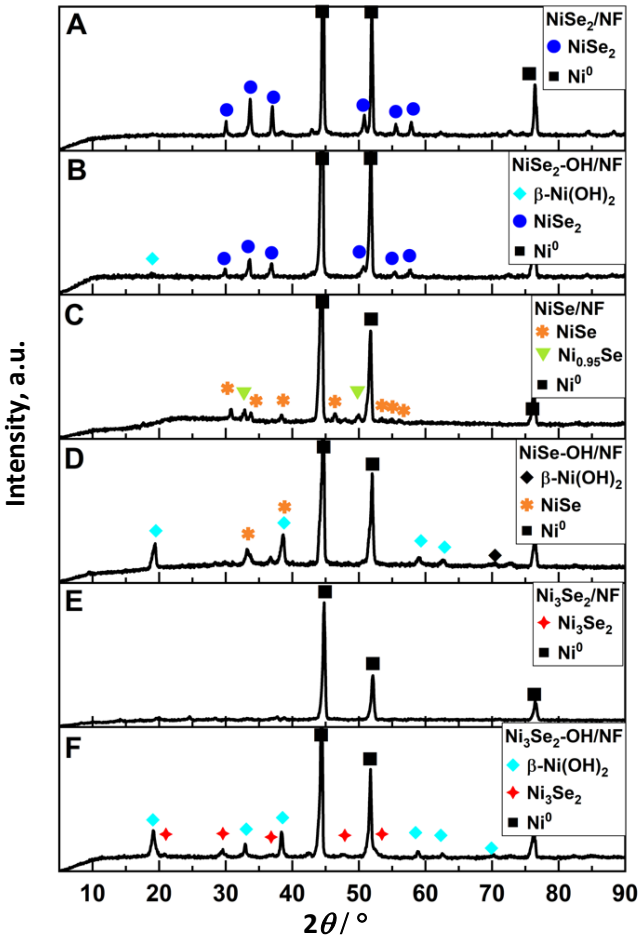

Figure 1. *XRD diffractograms of (A) $NiSe_2$/NF, (B) $NiSe_2$-OH/NF, (C) NiSe/NF, (D) NiSe-OH/NF, (E) Ni_3Se_2/NF, and (F) Ni_3Se_2-OH/NF*

The latter shows reflections at 2θ = 20.9, 29.6, 30.0, 36.6, 37.2, 42.6, 47.7, 48.2, 52.5 and 52.8°, indexed to {101}, {110}, {012}, {021}, {003, {202}, {211}, {113}, {300} and {122} crystallographic planes. The absence of NiO signals indicates that the $Ni(OH)_2$ dehydration did not occur during selenization at 550 °C.

According to the Ni-Se phase diagram, Ni_3Se_2 typically forms under Ni-deficient conditions [34]; however, in this case, the non-homogeneous distribution and limited Se vapor-Ni contact facilitated Ni_3Se_2 formation. The proposed mechanism for the formation of Ni_3Se_2-OH/NF initiates above 220 °C,

where elemental selenium begins to sublime and reacts with Ni to form NiSe. Then, NiSe reacts with metallic Ni to produce Ni_3Se_2. The overall transformation can be described by Equations (13) and (14):

$$Ni_{(s)} + Se_{(g)} \rightarrow NiSe_{(s)} \quad (13)$$

$$Ni_{(s)} + 2NiSe_{(s)} \rightarrow Ni_3Se_{2(s)} \quad (14)$$

SEM imaging (Figure 2) provides insights into the nanostructural evolution of the composites and supports the conclusions drawn from XRD analysis (Figure 2a), limiting the number of accessible catalytic sites. The $NiSe_2$-OH/NF sample developed urchin-like structures (Figure 2b), which inherently provide high surface area [35]; however, the overall material loading remained limited.

In contrast, the hydrothermal synthesis of NiSe/NF using NaBH4 yielded densely packed nanorods that fully covered the substrate (Figure 2c). This interconnected network shortens ion diffusion pathways and facilitates efficient charge transfer.

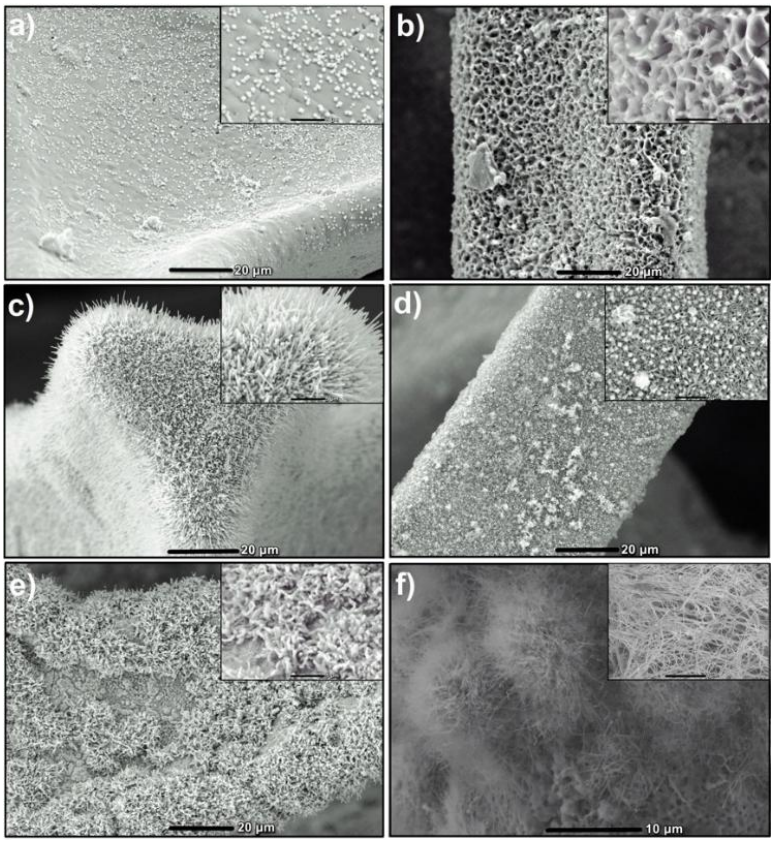

***Figure 2**. SEM micrographs of (a) $NiSe_2$/NF, (b) $NiSe_2$-OH/NF, (c) NiSe/NF, (d) NiSe-OH/NF, (e) Ni_3Se_2/NF and (f) Ni_3Se_2-OH/NF*

The NiSe-OH/NF material (Figure 2d) displayed a competition between NiSe and $Ni(OH)_2$ growth, as indicated by the increased formation of $Ni(OH)_2$ flakes that occupied key nucleation sites. Despite the reduced NiSe yield, the resulting particles were uniformly distributed throughout the 3D structure, forming a coherent hybrid heterostructure. Such architectures enhance active-site accessibility, promote strong electronic coupling, and aid gas evolution and electrolyte permeation [22,25].

A similar effect was observed in Ni_3Se_2/NF, where direct selenization produced dense, irregular agglomerates that were unevenly distributed (Figure 2e). However, when $Ni(OH)_2$/NF served as the substrate, highly elongated, uniformly distributed nanowires were formed (Figure 2f), demonstrating that $Ni(OH)_2$ modulates nucleation and growth kinetics.

To verify the elemental composition and spatial distribution of the synthesized catalysts, energy dispersive X-ray spectroscopy (EDS) mapping was performed. The Ni_3Se_2/NF and Ni_3Se_2-OH/NF electrodes were specifically selected for this analysis because they exhibited the weakest diffraction

intensities in the XRD patterns, necessitating confirmation that the constituent elements were uniformly deposited despite the structural disorder. As shown in Figure 3, the elemental maps demonstrate a highly homogeneous distribution of nickel and selenium across the entire scanned area. These results confirm that the synthesis process effectively covers the porous nickel foam architecture and indicate that the synthesis process effectively covers the porous nickel architecture and indicate that the weak XRD signals arise from the nanocrystalline or amorphous nature of the surface rather than insufficient material coverage.

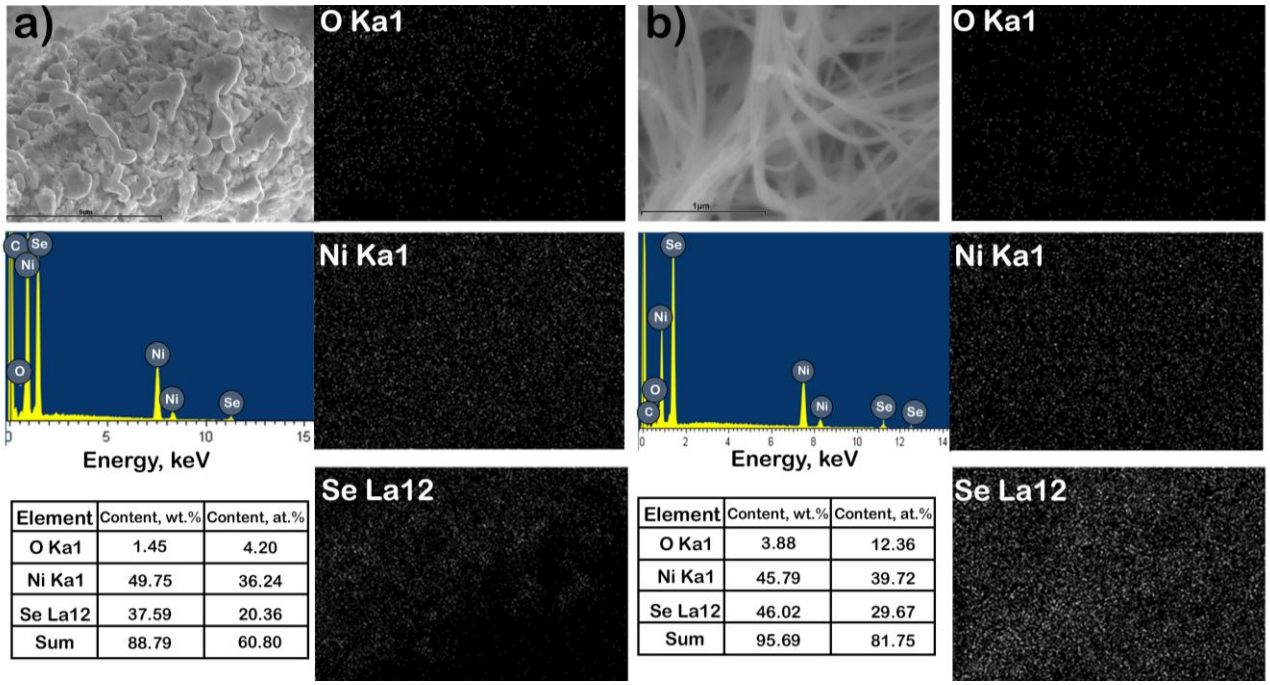

Element	Content, wt.%	Content, at.%
O Ka1	1.45	4.20
Ni Ka1	49.75	36.24
Se La12	37.59	20.36
Sum	88.79	60.80

Element	Content, wt.%	Content, at.%
O Ka1	3.88	12.36
Ni Ka1	45.79	39.72
Se La12	46.02	29.67
Sum	95.69	81.75

Figure 3. *SEM image, EDS spectra and elemental mapping (O, Ni, and Se) of (a) Ni_3Se_2/NF and (b) Ni_3Se_2-OH/NF*

The OER activity of all electrodes was evaluated in 1.0 M KOH by LSV at a scan rate of 5 mV s^{-1} (Figure 4a). For comparison, $NiSe_2$/NF, NiSe/NF, Ni_3Se_2/NF, bare NF and RuO_2 were tested under identical conditions. The LSV curves reveal the OER polarization behaviour of the various electrode configurations: $NiSe_2$/NF, $NiSe_2$-OH/NF, NiSe/NF, NiSe-OH/NF, Ni_3Se_2/NF, Ni_3Se_2-OH/NF, $Ni(OH)_2$/NF, bare NF and the RuO_2 benchmark. At a current density of 10 mA cm^{-2}, the corresponding overpotential values were 255, 229, 299, 177, 434, 410, 451, 390 and 379 mV, respectively. A pronounced enhancement in OER performance was observed for electrodes incorporating $Ni(OH)_2$, with the NiSe-OH/NF sample delivering the lowest overpotential of 177 mV at 10 mA cm^{-2}. This value is 202 mV lower than that of RuO_2, positioning this material as a highly competitive electrocatalyst. In addition, a substantial reduction of 122 mV compared to NiSe/NF highlights the critical role of the $Ni(OH)_2$ interlayer in facilitating electron transport and accelerating overall catalytic kinetics. Furthermore, benchmarking against representative literature reports (Figure 4) reveals that the NiSe-OH/NF electrode (177 mV at 10 mA cm^{-2}) exhibits lower overpotential than $NiSe_2$ (252 mV) and NiFe-MOF/$NiSe_x$/NF (198 mV), and improved or comparable performance relative to $NiCoSe_2$/NF (183 mV) and [NiFeSe]/Ni foil (191 mV) [6,15,36,20,32,37-46], further underscoring its competitive OER activity.

The enhanced performance can be attributed to the intimate phase coexistence and structural integration of $Ni(OH)_2$ within the nickel selenide-based composite framework, as supported by XRD analysis. This architecture promotes more efficient charge-transfer pathways and facilitates the

formation of the catalytically active NiOOH phase, which is associated with lower OER overpotentials and is evidenced by the redox feature at approximately 1.41 V.

This enhancement may further be attributed to the generation of oxygen vacancies within the $Ni(OH)_2$ lattice. These vacancies can form through the partial reduction of Ni during electrochemical oxidation, accompanied by the conversion of lattice oxygen (Ni-O) into molecular O_2 during the OER process [47]. Additionally, the strong covalent interaction between Ni and Se atoms facilitates delocalization of Ni 3d electrons during catalysis, contributing to the improved OER activity observed for NiSe-based materials [4].

The kinetics of the oxygen evolution reaction were examined through Tafel analysis based on the polarization curves obtained from LSV measurements. As shown in Figure 4c, the electrodes incorporating $Ni(OH)_2$ exhibit notably low Tafel slopes (44.1 to 69.1 mV dec^{-1}), indicative of favourable reaction kinetics. This behaviour is commonly associated with the formation of the absorbed intermediate species ($M\text{-}O_{ads}$), stabilized through weak van der Waals interactions, which facilitates the progression of the OER. The low slopes also suggest that the rate-determining step likely occurs during the final stage of the multielectron transfer sequence [48]. The theoretical Tafel slope for OER is approximately 40 mV dec^{-1}, which aligns well with the average of the experimental values, lending further support to this mechanistic interpretation.

Additionally, the $NiSe_2$/NF electrode exhibits a low Tafel slope of 50.1 mV dec^{-1}, which can be attributed to its high overall performance and optimized surface morphology, thereby enhancing active-site exposure. This trend is consistent with the presence of a well-defined faradaic feature corresponding to the $Ni(OH)_2$/NiOOH redox transition in the LSV profiles [26,49], further confirming the participation of this redox couple in the catalytic process.

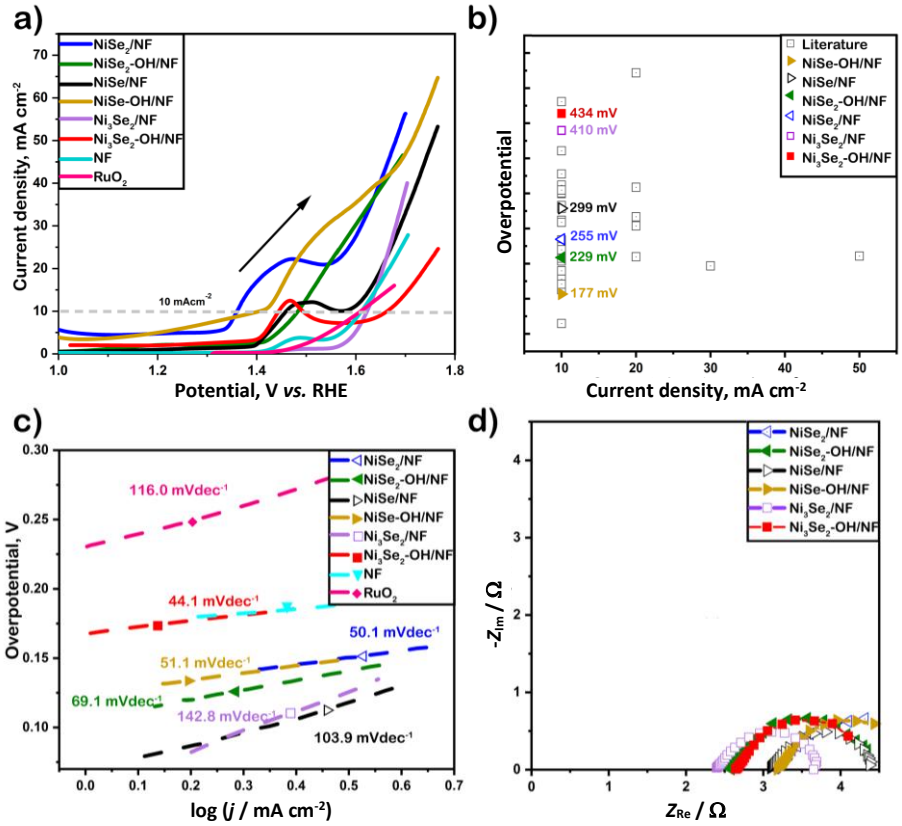

Figure 4. *(a) Linear sweep voltammograms of the composites, bare NF and RuO_2 in 1.0 M KOH, (b) comparison between OER overpotentials for the synthesized catalysts and previously reported nickel-based selenides, (c) Tafel plots derived from LSV data of all electrodes, (d) Nyquist plots of NiSe/NF, NiSe-OH/NF, $NiSe_2$/NF, $NiSe_2$-OH/NF, Ni_3Se_2/N, and Ni_3Se_2-OH/NF*

Electrochemical impedance spectroscopy (EIS) was employed to deepen the mechanistic understanding of charge-transfer processes under OER conditions. Figure 4d presents the Nyquist plots for all catalysts (NiSe/NF, NiSe-OH/NF, $NiSe_2$/NF, $NiSe_2$-OH/NF, Ni_3Se_2/NF and Ni_3Se_2-OH/NF), where Z_{Re} and Z_{Im} represent the real and imaginary components, respectively. The semicircular diameter at high frequencies associated with the charge-transfer resistance (R_{ct}) provides direct insight into interfacial electron transfer. Measurements conducted at 1.63 V *vs*. RHE, in the frequency range of 100 kHz to 20 mHz ensured that all electrodes were evaluated under active OER conditions.

The data obtained from the impedance test were fitted to an equivalent circuit with a series resistance coupled to a constant phase with a parallel resistance (Randles circuit). The R_{ct} values for NiSe/NF, NiSe-OH/NF, $NiSe_2$/NF, $NiSe_2$-OH/NF, Ni_3Se_2/NF, and Ni_3Se_2-OH/NF were 1.32, 2.05, 1.84, 2.20, 1.29 and 1.82 Ω, respectively. The slight increase in R_{ct} observed for the $Ni(OH)_2$ containing electrodes is consistent with the semiconducting character of $Ni(OH)_2$. However, this minor increase in resistance is effectively compensated by enhanced reaction kinetics, as evidenced by the lower Tafel slopes discussed previously (Figure 4c). This indicates that the heterostructure facilitates a more efficient reaction mechanism despite the lower conductivity. Nevertheless, all R_{ct} values fall within the low range of 1 to 2 Ω. Importantly, the $Ni(OH)_2$ interlayer provides additional advantages, including improved active-site accessibility and enhanced structural stability during OER operation.

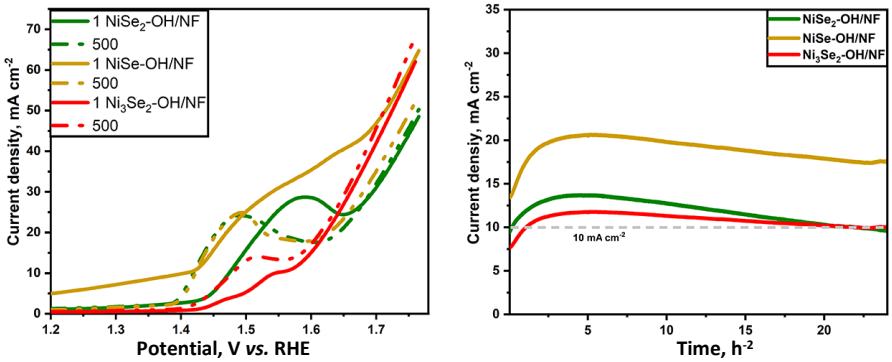

Figure 5. *(a) OER LSVs at 1st and 500th cycles of cyclic voltammetry, and (b) chronoamperometry tests of NiSe-OH/NF, $NiSe_2$-OH/NF, Ni_3Se_2-OH/NF*

In addition to exhibiting excellent initial electrochemical activity, long-term stability is critical for practical water-splitting applications. Durability is commonly assessed using cyclic voltammetry, cycling and chronoamperometry measurements. The overlaid LSV curves recorded before and after 500 CV cycles (Figure 5a) show minimal degradation in current density, indicating strong electrochemical stability during OER. The small changes observed at approximately 1.40 and 1.60 V *vs*. RHE are attributed to the evolution of the $Ni(OH)_2$/NiOOH redox couple, which becomes increasingly active upon prolonged cycling.

To further evaluate operational stability under continuous electrolysis, chronoamperometry was performed at a constant potential of 1.60 V *vs*. RHE for 24 h. Both NiSe-OH/NF and Ni_3Se_2-OH/NF maintained high current densities of 17.60 and 10.05 mA cm^{-2}, respectively, retaining over 86 % of their maximum current density (Figure 5b). A slight performance decay was observed for $NiSe_2$-OH/NF, which stabilized at 9.58 mA cm^{-2}, but still preserved a substantial portion of its catalytic activity after 24 h.

Post-catalytic characterization was conducted to verify the durability of the electrode [9]. As shown in Figure 6, the diffraction peaks of the post-OER sample closely match those of the pristine material, indicating that the crystalline structure remains stable under harsh oxidative conditions.

Notably, a reduction in overall crystallinity is observed, as evidenced by broader, less intense diffraction peaks. This structural evolution suggests that, while the crystalline core remains intact, the surface undergoes partial amorphization, likely induced by the in-situ formation of amorphous metal oxyhydroxide and oxide species such as NiO_2, which are widely recognized as common phenomena with all metal selenide electrocatalysts [26].

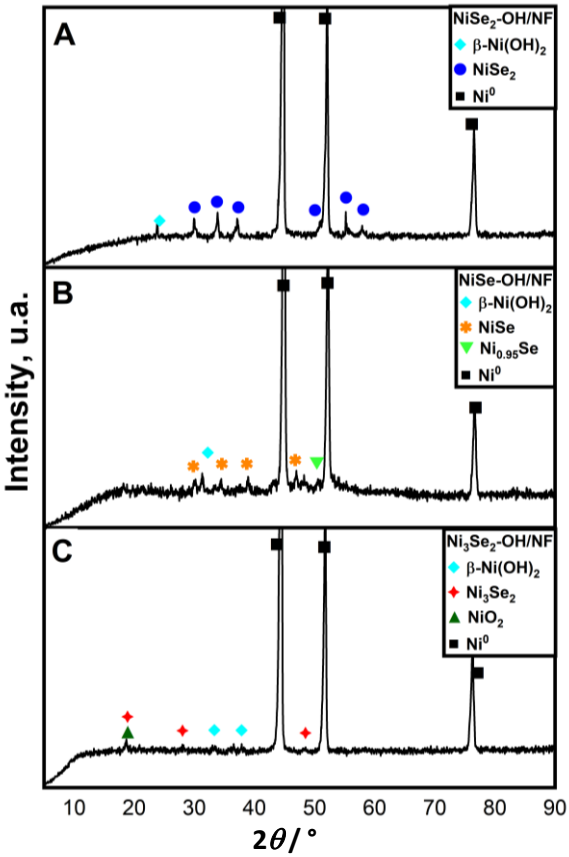

Figure 6. *XRD of (a) NiSe-OH/NF, (b) $NiSe_2$-OH/NF, and (c) Ni_3Se_2-OH/NF after 24 h of chronoamperometry test*

The observed structural stability and surface reconstruction highlight the superior durability of the catalyst. In particular, the nickel selenide-based framework, coupled with the $Ni(OH)_2$ interlayer architecture, facilitates efficient electron transport and enhances the stability of catalytically active sites, rendering this material a promising candidate for long-term alkaline OER applications.

Conclusions

In summary, this study presented a comprehensive evaluation of several nickel selenide phases: $NiSe_2$, NiSe and Ni_3Se_2, and their corresponding $Ni(OH)_2$-modified heterostructures, revealing the strong influence of phase composition and interfacial engineering on OER performance. Structural and morphological analyses confirmed that the presence of $Ni(OH)_2$ modified the nucleation process, enhanced material distribution within 3D Ni foam, and promoted the formation of well-integrated heterostructures. Electrochemical measurements demonstrated that $Ni(OH)_2$ incorporation consistently improved catalytic performance across all nickel selenide systems. The NiSe-OH/NF electrode exhibited the most outstanding activity, achieving an overpotential of only 177 mV at 10 mA cm^{-2}, along with favourable kinetic parameters and exceptional stability. These enhancements can be attributed to optimized charge-transfer pathways, the activation of the $Ni(OH)_2$/NiOOH redox couple, and the synergistic electronic effects arising from Ni-Se interactions. The $NiSe_2$- and Ni_3Se_2-based heterostructures also showed notable improvements compared to their unmodified forms, further

demonstrating the versatility and effectiveness of $Ni(OH)_2$ interfacial modulation. Overall, the results highlight the critical role of phase selection and interface engineering in improving the intrinsic and operational performance of nickel selenide electrocatalysts. This work offers valuable insights for the rational design of cost-effective, earth-abundant OER catalysts and contributes to the advancement of sustainable hydrogen-production technologies.

***Conflict of interest*:** The authors have no conflict of interest.

Acknowledgements: *The authors gratefully acknowledge Secithi for the scholarship granted.*

Funding: *Universidad Autónoma de Nuevo León (UANL)*

References

[1] S.G. Nnabuife, A.K. Hamzat, J. Whidborne, B. Kuang, K.W. Jenkins, Integration of renewable energy sources in tandem with electrolysis: A technology review for green hydrogen production, *International Journal of Hydrogen Energy* **107** (2025) 218-240. https://doi.org/10.1016/j.ijhydene.2024.06.342

[2] A. Małek, Low-Emission Hydrogen for Transport—A Technology Overview from Hydrogen Production to Its Use to Power Vehicles, *Energies* **18** (2025) 4425 https://doi.org/10.3390/en18164425

[3] S. Abouricha, H. Aziam, H. Noukrati, O. Sel, I. Saadoune, M. Lahcini, H.B. Youcef, Biopolymers-Based Proton Exchange Membranes For Fuel Cell Applications: A Comprehensive Review, *ChemElectroChem* **11** (2024) e202300648. https://doi.org/10.1002/celc.202300648

[4] Z. Chen, T. Zhou, Q. Liu, Z. Wang, R. Gu, L. Guo, Y. Liu, Three-Dimensional Flower-Like Bimetallic Nickel-Iron Selenide for Efficient Oxygen Evolution Reaction, *The Journal of Physical Chemistry C* **126** (2022) 5131-5137. https://doi.org/10.1021/acs.jpcc.1c09962

[5] T.B. Ferriday, P.H. Middleton, Alkaline fuel cell technology - A review, *International Journal of Hydrogen Energy* **46** (2021) 18489-18510. https://doi.org/10.1016/j.ijhydene.2021.02.203

[6] Z. Feng, H. Zhang, L. Wang, B. Gao, P. Lu, P. Xing, Nanoporous nickel-selenide as high-active bifunctional electrocatalyst for oxygen evolution and hydrazine oxidation, *Journal of Electroanalytical Chemistry* **876** (2020) 114740. https://doi.org/10.1016/j.jelechem.2020.114740

[7] Q. Sun, M. Zhou, Y. Shen, L. Wang, Y. Ma, Y. Li, X. Bo, Z. Wang, C. Zhao, Hierarchical nanoporous Ni(Cu) alloy anchored on amorphous NiFeP as efficient bifunctional electrocatalysts for hydrogen evolution and hydrazine oxidation, *Journal of Catalysis* **373** (2019) 180-189. https://doi.org/10.1016/j.jcat.2019.03.039

[8] B. Jin, J. Sainio, J. Shi, H. Jiang, B. Ali, N. Han, T. Kallio, Bifunctional surface-distributed RuO2 on NiFe double layer hydroxide for efficient alkaline water splitting, *Chemical Engineering Journal* **520** (2025) 165999. https://doi.org/10.1016/j.cej.2025.165999

[9] A.T. Swesi, J. Masud, M. Nath, Nickel selenide as a high-efficiency catalyst for oxygen evolution reaction, *Energy & Environmental Science* **9** (2016) 1771-1782. https://doi.org/10.1039/C5EE02463C

[10] S. Anantharaj, S. Kundu, S. Noda, Progress in nickel chalcogenide electrocatalyzed hydrogen evolution reaction, *Journal of Materials Chemistry A* **8** (2020) 4174-4192. https://doi.org/10.1039/C9TA14037A

[11] F.F. Alharbi, H.M.T. Farid, A Nanosized Manganese-Based Chalcogenide Composite for Enhanced Electrocatalytic OER, *Journal of Electronic Materials* **52** (2023) 3661-3671. https://doi.org/10.1007/s11664-023-10330-z

[12] S. Aslam, S. Ahmed, M. Safdar, A Mini-Review of Electrocatalysts Assembled with Transition Metal Chalcogenides for Overall Water Splitting, *Journal of Electronic Materials* **54** (2025) 8144-8165. https://doi.org/10.1007/s11664-025-12224-8

[13] M.R. Kandel, U.N. Pan, D.R. Paudel, P.P. Dhakal, N.H. Kim, J.H. Lee, Hybridized bimetallic phosphides of Ni-Mo, Co-Mo, and Co-Ni in a single ultrathin-3D-nanosheets for efficient HER and OER in alkaline media, *Composites Part B: Engineering* **239** (2022) 109992. https://doi.org/10.1016/j.compositesb.2022.109992

[14] M.A.R. Anjum, M.S. Okyay, M. Kim, M.H. Lee, N. Park, J.S. Lee, Bifunctional sulfur-doped cobalt phosphide electrocatalyst outperforms all-noble-metal electrocatalysts in alkaline electrolyzer for overall water splitting, *Nano Energy* **53** (2018) 286-295. https://doi.org/10.1016/j.nanoen.2018.08.064

[15] S. Esmailzadeh, T. Shahrabi, Y. Yaghoubinezhad, Gh. Barati Darband, Optimization of nickel selenide for hydrogen and oxygen evolution reactions by response surface methodology, *Journal of Colloid and Interface Science* **600** (2021) 324-337. https://doi.org/10.1016/j.jcis.2021.05.003

[16] Z. Guo, R. Zhao, S. Yan, W. Xiong, J. Zhu, K. Lu, X. Wang, Atomic Layer Deposition of $FeSe_2$, $CoSe_2$, and $NiSe_2$, *Chemistry of Materials* **33** (2021) 2478-2487. https://doi.org/10.1021/acs.chemmater.0c04708

[17] S. Chen, J.-L. Mi, P. Zhang, Y.-H. Feng, Y.-C. Yong, W.-D. Shi, Control Synthesis of Nickel Selenides and Their Multiwalled Carbon Nanotubes Composites as Electrocatalysts for Enhanced Water Oxidation, *The Journal of Physical Chemistry C* **122** (2018) 26096-26104. https://doi.org/10.1021/acs.jpcc.8b09259

[18] M. Ghaemmaghami, Y. Yamini, E. Saievar-Iranizad, A. Bayat, Straightforward fabrication of robust Fe-doped Ni_3 Se_2 supported nickel foam as a highly efficient electrocatalyst for the oxygen evolution reaction, *Sustainable Energy & Fuels* **4** (2020) 1150-1156. https://doi.org/10.1039/C9SE00896A

[19] R. Briones-Martínez, N.A. Garcia-Gomez, S. Sepúlveda-Guzmán, S.M. De La Parra-Arciniega, E.M. Sánchez, Self-supported Ni_3Se_2/$Ni(OH)_2$ and Ni_3Se_2 on Ni-foam: nanostructured arrays for the hydrogen evolution reaction, *Journal of Nanoparticle Research* **22** (2020) 356. https://doi.org/10.1007/s11051-020-05088-y

[20] M. Saquib, P. Arora, A.C. Bhosale, Nickel molybdenum selenide on carbon cloth as an efficient bifunctional electrocatalyst for alkaline seawater splitting, *Fuel* **365** (2024) 131251. https://doi.org/10.1016/j.fuel.2024.131251

[21] F. Hiege, C.-W. Chang, O. Trost, C.E.R. Van Halteren, P. Hosseini, G. Bendt, S. Schulz, Z. Feng, J. Linnemann, K. Tschulik, Morphological Degradation of Oxygen Evolution Reaction-Electrocatalyzing Nickel Selenides at Industrially Relevant Current Densities, *ACS Applied Materials & Interfaces* **17** (2025) 41893-41903. https://doi.org/10.1021/acsami.5c05381

[22] S.-J. Huang, S. Balu, N.R. Barveen, R. Sankar, Surface engineering of reduced graphene oxide onto the nanoforest-like nickel selenide as a high performance electrocatalyst for OER and HER, *Colloids and Surfaces A: Physicochemical and Engineering Aspects* **654** (2022) 130024. https://doi.org/10.1016/j.colsurfa.2022.130024

[23] M. Arabi, A. Ghaffarinejad, G.B. Darband, Electrodeposition of nanoporous nickel selenide on graphite rod as a bifunctional electrocatalyst for hydrogen and oxygen evolution reactions, *Journal of Electroanalytical Chemistry* **907** (2022) 116066. https://doi.org/10.1016/j.jelechem.2022.116066

[24] S. Liu, Y. Jiang, M. Yang, M. Zhang, Highly conductive and metallic cobalt-nickel selenide nanorods supported on Ni foam as an efficient electrocatalyst for alkaline water splitting, *Nanoscale* **11** (2019) 7959-7966. https://doi.org/10.1039/C8NR10545F

[25] C. Zhang, Y. Zhang, S. Zhou, C. Li, Self-supported iron-doping $NiSe_2$ nanowrinkles as bifunctional electrocatalysts for electrochemical water splitting, *Journal of Alloys and Compounds* **818** (2020) 152833. https://doi.org/10.1016/j.jallcom.2019.152833

[26] S. Anantharaj, E. Subhashini, K.C. Swaathini, T.S. Amarnath, S. Chatterjee, K. Karthick, S. Kundu, Respective influence of stoichiometry and NiOOH formation in hydrogen and oxygen evolution reactions of nickel selenides, *Applied Surface Science* **487** (2019) 1152-1158. https://doi.org/10.1016/j.apsusc.2019.05.118

[27] N.I. Watson, M. Keegan, B. Van Den Bosch, N. Yan, G. Rothenberg, The Influence of Metal Impurities on NiOOH Electrocatalytic Activity in the Oxygen Evolution Reaction, *ChemElectroChem* **11** (2024) e202400223. https://doi.org/10.1002/celc.202400223

[28] A.T. Swesi, J. Masud, W.P.R. Liyanage, S. Umapathi, E. Bohannan, J. Medvedeva, M. Nath, Textured NiSe2 Film: Bifunctional Electrocatalyst for Full Water Splitting at Remarkably Low Overpotential with High Energy Efficiency, *Scientific Reports* **7** (2017) 2401. https://doi.org/10.1038/s41598-017-02285-z

[29] International Centre for Diffraction Data (ICDD), PDF-2 Database, Release 2024, Newtown Square, PA, USA.

[30] T. Bhandari, R. Kafle, P. Ban, J. Ghorsine, D. Acharya, D.R. Paudel, Environmentally benign synthesis of CuO impregnated activated carbon nanocomposite for prompt bifunctional water splitting applications: Original scientific paper, *Journal of Electrochemical Science and Engineering* **16** (2026) 3012. https://doi.org/10.5599/jese.3012

[31] Y. Rao, Y. Wang, H. Ning, P. Li, M. Wu, Hydrotalcite-like $Ni(OH)_2$ Nanosheets in Situ Grown on Nickel Foam for Overall Water Splitting, *ACS Applied Materials & Interfaces* **8** (2016) 33601-33607. https://doi.org/10.1021/acsami.6b11023

[32] J. Xu, J. Zhou, L. Yuan, L. Song, Combinational modulations of $NiSe_2$ nanodendrites by phase engineering and iron-doping towards efficient oxygen evolution reaction, *Journal of Materials Chemistry A* **8** (2020) 4948-4954. https://doi.org/10.1039/D0TA00860E

[33] H.-B. Wang, Y.-S. Sun, F. Ma, L. Zhou, H.-F. Li, L. Zhang, G.-J. Chen, Y.-K. Xu, Y.-N. Chen, K.-W. Xu, D.-Y. Ma, Se molarity tuned composition and configuration of Ni_3Se_2/NiSe core-shell nanowire heterostructures for hydrogen evolution reaction, *Journal of Alloys and Compounds* **819** (2020) 153056. https://doi.org/10.1016/j.jallcom.2019.153056

[34] B. Yuan, W. Luan, S. Tu, One-step solvothermal synthesis of nickel selenide series: Composition and morphology control, *CrystEngComm* **14** (2012) 2145-2151. https://doi.org/10.1039/c2ce06474j

[35] Z. Rahmati, M. Roushani, H. Hosseini, Hierarchical hollow sea-urchin-like Ni-Co diselenide encapsulated in N-doped carbon networks as an advanced core-shell bifunctional electrocatalyst for fabrication of nonenzymatic glucose and hydrogen peroxide sensors, *Sensors and Actuators B: Chemical* **324** (2020) 128730. https://doi.org/10.1016/j.snb.2020.128730

[36] K. Akbar, J.H. Jeon, M. Kim, J. Jeong, Y. Yi, S.-H. Chun, Bifunctional Electrodeposited 3D $NiCoSe_2$ /Nickle Foam Electrocatalysts for Its Applications in Enhanced Oxygen Evolution Reaction and for Hydrazine Oxidation, *ACS Sustainable Chemistry & Engineering* **6** (2018) 7735-7742. https://doi.org/10.1021/acssuschemeng.8b00644

[37] S. Xu, J. Du, J. Li, L. Sun, F. Li, Nickel-selenide templated binary metal-organic frameworks for efficient water oxidation, *Journal of Materials Chemistry A* **8** (2020) 16908-16912. https://doi.org/10.1039/D0TA00785D

[38] J. Du, Z. Zou, C. Liu, C. Xu, Hierarchical Fe-doped Ni_3Se_4 ultrathin nanosheets as an efficient electrocatalyst for oxygen evolution reaction, *Nanoscale.* **10** (2018) 5163-5170 https://doi.org/10.1039/C8NR00426A

[39] S. Kim, H. Yoo, Construction of a Pliable Electrode System for Effective Electrochemical Oxygen Evolution Reaction: Direct Growth of Nickel/Iron/Selenide Nanohybrids on Nickel Foil, *ACS Sustainable Chemistry & Engineering* **8** (2020) 13859-13867. https://doi.org/10.1021/acssuschemeng.0c05857

[40] B.M. Mohanty, B. Kumar, M. Kandasamy, N. Dalai, R. Kumar, B. Chakraborty, J. Bijayalaxmi, The role of Se vacancy and Fe doping on Nickel Selenide for Water Oxidation Reaction, *Sustainable Energy & Fuels* **4** (2020) 3058-3065. https://doi.org/10.1039/C7SE00062F

[41] Z. Pan, Z. Tang, M. Yaseen, Y. Zhan, NiSe and Fe-Based Layerd Double Hydroxide Nanosheet/Ni Foam Bifunctional Catalyst for Water Splitting, *ACS Applied Nano Materials* **5** (2022) 16793-16803. https://doi.org/10.1021/acsanm.2c03764

[42] W. Bao, J. You, Y. Zhao, L. Wang, R. Yao, Enhanced oxygen evolution reaction activity of $Ni(OH)_2$ nanosheets via the modified effect of sulfur, *Journal of Chemical Sciences* **134** (2022) 76. https://doi.org/10.1007/s12039-022-02072-y

[43] Z. Alhalili, M. Shariq, N. Al-Qasmi, O. Hakami, H.J. Alathlawi, A.F. Alharbi, E.A. Mergani, E.A. Elghazali, A.I. Elghazali, I. Mahariq, Enhanced catalytic activity of $NiSe_2$ by nanohybrid formation with CoO nanosheets towards overall electrocatalytic water splitting for clean energy, *International Journal of Hydrogen Energy* **94** (2024) 997-1004. https://doi.org/10.1016/j.ijhydene.2024.11.147

[44] Y. Li, H. Du, Y. Su, J. Zhao, K. Qu, X. Zhang, Y. Zhang, Y. Dong, Z. Guo, Construction of Heterostructured NiS/NiSe2 and their application in electrocatalytic water splitting, *International Journal of Hydrogen Energy* **66** (2024) 286-293. https://doi.org/10.1016/j.ijhydene.2024.04.101

[45] H. Xue, T. Yang, Z. Zhang, Y. Zhang, Z. Geng, Y. He, Stimulate the hidden catalysis potential and exposure of nickel site in NiSe@CNTs result in ultra-high HER/OER activity and stability, *Applied Catalysis B: Environmental* **330** (2023) 122641. https://doi.org/10.1016/j.apcatb.2023.122641

[46] X. Han, H. Qian, Y. Zhao, J. Ji, Z. Cao, P. Zhu, X. Zhao, S. Liu, Carbon nanotubes entangled nickel diselenides with S doping and Se vacancy for enhanced oxygen evolution reaction, *Journal of Power Sources* **645** (2025) 237226. https://doi.org/10.1016/j.jpowsour.2025.237226

[47] X. Zheng, Y. Cao, X. Han, H. Liu, J. Wang, Z. Zhang, X. Wu, C. Zhong, W. Hu, Y. Deng, Pt embedded Ni_3Se_2@NiOOH core-shell dendrite-like nanoarrays on nickel as bifunctional electrocatalysts for

overall water splitting, *Science China Materials* **62** (2019) 1096-1104. https://doi.org/10.1007/s40843-019-9413-5

[48] T. Shinagawa, A.T. Garcia-Esparza, K. Takanabe, Insight on Tafel slopes from a microkinetic analysis of aqueous electrocatalysis for energy conversion, *Scientific Reports* **5** (2015) 13801. https://doi.org/10.1038/srep13801

[49] C. Zhang, Z. Xie, Y. Liang, D. Meng, Z. Wang, X. He, W. Qiu, M. Chen, P. Liang, Z. Zhang, Morphological and compositional modification of β-$Ni(OH)_2$ nanoplates by ferrihydrite for enhanced oxygen evolution reaction, *International Journal of Hydrogen Energy* **46** (2021) 17720-17730. https://doi.org/10.1016/j.ijhydene.2021.02.173